ACS APPLIED MATERIALS & INTERFACES

www.acsami.org

Research Article

Electrochemical Activation of $LiGaO_2$: Implications for Ga-Doped Garnet Solid Electrolytes in Li-Metal Batteries

Anna Windmüller,* Kristian Schaps, Frederik Zantis, Anna Domgans, Bereket Woldegbreal Taklu, Tingting Yang, Chih-Long Tsai, Roland Schierholz, Shicheng Yu, Hans Kungl, Hermann Tempel, Rafal E. Dunin-Borkowski, Felix Hüning, Bing Joe Hwang, and Rüdiger-A. Eichel

Cite This: ACS Appl. Mater. Interfaces 2024, 16, 39181−39194

Read Online

ACCESS | Metrics & More | Article Recommendations | Supporting Information

ABSTRACT: Ga-doped $Li_7La_3Zr_2O_{12}$ garnet solid electrolytes exhibit the highest Li-ion conductivities among the oxide-type garnet-structured solid electrolytes, but instabilities toward Li metal hamper their practical application. The instabilities have been assigned to direct chemical reactions between $LiGaO_2$ coexisting phases and Li metal by several groups previously. Yet, the understanding of the role of $LiGaO_2$ in the electrochemical cell and its electrochemical properties is still lacking. Here, we are investigating the electrochemical properties of $LiGaO_2$ through electrochemical tests in galvanostatic cells versus Li metal and complementary *ex situ* studies via confocal Raman microscopy, quantitative phase analysis based on powder X-ray diffraction, energy-dispersive X-ray spectroscopy, X-ray photoelectron spectroscopy, and electron energy loss spectroscopy. The results demonstrate considerable and surprising electrochemical activity, with high reversibility. A three-stage reaction mechanism is derived, including reversible electrochemical reactions that lead to the formation of highly electronically conducting products. The results have considerable implications for the use of Ga-doped $Li_7La_3Zr_2O_{12}$ electrolytes in all-solid-state Li-metal battery applications and raise the need for advanced materials engineering to realize Ga-doped $Li_7La_3Zr_2O_{12}$for practical use.

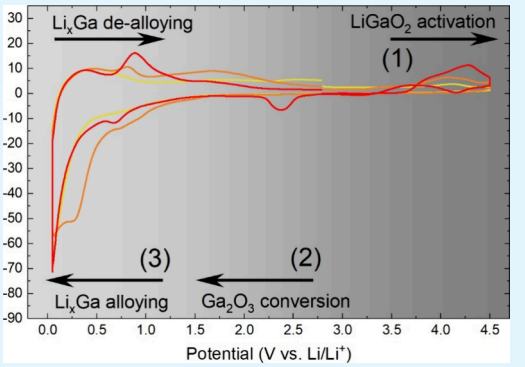

KEYWORDS: *$LiGaO_2$, garnet solid electrolyte, Ga-doping, $Li_7La_3Zr_2O_{12}$, solid-state battery*

INTRODUCTION

Garnet-structured solid electrolytes enable all-solid-state Li-metal batteries (ASSLMBs) to have the potential to enhance the safety and energy density of ASSLMBs significantly in comparison to conventional Li-ion batteries (LIB).[1−3] Among the family of garnet-structured solid electrolytes derived from $Li_7La_3Zr_2O_{12}$ (LLZO), Ga-doped LLZO (Ga:LLZO) shows the highest Li-ion conductivity at room temperature, exceeding 1 mS cm^{-1}.[1,4,5] Ga:LLZO thus receives a lot of interest and is intensely studied for its relation of crystal chemistries, structures and ionic conductivities,[6−11] structural stabilization for optimizing its conductivities,[12,13] sintering optimization for creating dense ceramics with high purity,[7,14−16] thin film deposition for the application as thin film electrolyte,[17] and application as a thick film for solid-state battery fabrications.[4,5,13,14] In general, it has been found that optimized conductivities >1 mS cm^{-1} at room temperature can be achieved through the stabilization of the cubic garnet phase at low levels of Ga-doping, that is, $0.2 < x < 0.3$ in $Li_{7-3x}Ga_xLa_3Zr_2O_{12}$, while $6.4 < Li < 6.6$.[6,11,15,17]

For higher Ga substitutions ($x > 0.5$ mol per formula unit of LLZO), β-$LiGaO_2$ emerges as an obvious secondary phase in Ga:LLZO that can be detected by X-ray diffraction[7,9,10] and at the grain boundaries of the garnet phase by electron microscopy.[6] However, studies employing transmission and electron microscopy have recently demonstrated that even at considerably low Ga-doping levels (<0.1 mol per formula unit of LLZO), $LiGaO_2$ can be found at grain boundaries and in triple junctions in the densified Ga:LLZO ceramic pellets.[4,5,13] At the same time, it has been reported that $LiGaO_2$ accumulation on the grain boundary can be correlated to the instability of Ga:LLZO toward Li metal.[4,5,13] For example, Li et al. reported severe cracking once Ga:LLZO pellet is in contact with molten Li.[13] In an attempt to study the reaction mechanism, $LiGaO_2$ was reacted with liquid Li metal, where Li_2Ga and Li_2O formation was observed. The huge volume expansion from these educts to products was thus identified as the cause of the microstructural cracking to collapse $LiGaO_2$

Received: March 5, 2024
Revised: June 15, 2024
Accepted: July 10, 2024
Published: July 16, 2024

containing Ga:LLZO pellets when in contact with molten Li metal.[13]

Various efforts were undertaken to control and eliminate the presence of $LiGaO_2$ phases in Ga:LLZO to improve the stability of Ga:LLZO against Li metal effectively. Su et al. found that the presence of $LiGaO_2$ is related to abnormal grain growth of LLZO particles during sintering.[16] They developed a processing strategy via a two-step sintering leading to fine grains of Ga:LLZO after the sintering process and thus avoiding $LiGaO_2$ secondary phase formation to improve the stability against Li metal.[16] Li et al. reported to control and suppress the secondary $LiGaO_2$ phase formation by adding 2 wt % SiO_2 into Ga:LLZO powder during the sintering process.[13] This resulted in improved thermomechanical and electrochemical stability when in contact with molten Li. It is hypothesized that SiO_2 extracts Li from $LiGaO_2$ to form Li_2SiO_3 while the remaining Ga incorporates into the LLZO bulk.[13]

In one of our previous studies, we compared and analyzed the reactions between Li metal and sintered $Li_{6.4}Ga_{0.2}La_3Zr_2O_{12}$ and $Li_{6.45}Ga_{0.05}La_3Zr_{1.6}Ta_{0.4}O_{12}$, in comparison to Ga-free $Li_{6.45}Al_{0.05}La_3Zr_{1.6}Ta_{0.4}O_{12}$ (Ta:LLZO). We demonstrated that Ga:LLZO undergoes chemical reactions with Li metal, while Ta:LLZO remains stable. In this study, we could also demonstrate that Ga from the Ga:LLZO bulk forms Li−Ga alloys at the grain boundaries of the Ga:LLZO ceramic after reaction with molten Li. By NMR measurements, it was proven that Ga-ions can leach out from the bulk into the grain boundary after contacting Li metal.[4,5] The primary observation of Ga leaching into the grain boundaries of the Ga:LLZO ceramic questions the actual role of $LiGaO_2$ in the failure mechanism of the Ga:LLZO solid electrolyte.

In the literature, β-$LiGaO_2$ is well-known in the area of semiconductor research and semiconductor industry, where it serves as a substrate for GaN growth.[18] β-$LiGaO_2$ itself can be grown into rather large single crystals,[18,19] and its crystal structure was determined by Marezio in 1964 to be identical to that of orthorhombic β-$NaFeO_2$.[20] Therefore, its structural, optical, and electrical properties are well understood,[21−24] but it is hard to extrapolate, which role $LiGaO_2$ may play in the instability of Ga:LLZO toward Li, even in an isolated environment without physical contact to Li. Furthermore, its stability and reactions under a larger electrochemical voltage, such as in a full battery cell, are not yet understood. Here, we investigate $LiGaO_2$ from an electrochemical point of view to understand the possible impact of β-$LiGaO_2$ in Ga:LLZO ceramics under dynamic conditions, i.e., under an applied electrical field and electrochemical cycling conditions, as in a battery. To accomplish this, we synthesize β-$LiGaO_2$ and examine it as the positive electrode in a galvanic cell for understanding its electrochemical properties. The results contribute to a better understanding of the Ga:LLZO failure mechanism when in contact with Li metal, which may offer a better strategy for fabricating and processing the Ga:LLZO solid electrolyte for ASSLMB application.

EXPERIMENTAL SECTION

$LiGaO_2$ Synthesis and Electrode Preparation. An adapted version of the Ga:LLZO synthesis procedure was used to produce $LiGaO_2$ powder.[4] The synthesis was performed by mixing Li_2CO_3 and Ga_2O_3 powders in an autogrinder (Retsch) in a 1:1 ratio, adding a slight excess of Li_2CO_3(10 wt %) to compensate for Li-evaporation losses. The powder mixture was heated to a temperature of 1200 °C with a heating ramp of 5 K min^{-1} in a muffle furnace in air in a closed corundum crucible. The reaction product was cooled freely after 8 h and reground in the autogrinder to produce a fine powdered sample.

To test the powder for its electrochemical activity, it was processed by a typical laboratory-scale procedure into an electrode tape with a 10:10:80 ratio of polyvinylidene difluoride (PvDF, Alfa-Aesar): carbon black: $LiGaO_2$.[13] Prior to the slurry preparation, carbon black powder (Super P, Alfa-Aesar) and $LiGaO_2$ powder were dried in a vacuum furnace at 80 °C for 16 h. The powder was mixed and ground in a mortar for more than 20 min. The mixture was added to polyvinylidene difluoride (PvDF), dissolved in *N*-methylpyrrolidone (NMP, Alfa-Aesar), and stirred vigorously for 5 h. The slurry was drop-coated on a ⌀11 mm Ni current collector and dried for at least 24 h in a hood, following another 24 h in a vacuum oven at 80 °C. The final electrode has a mass loading of ∼5 mg, as determined for every sample by weighting the nickel plate before coating and the nickel plate plus coating individually.

Electrochemical Measurements. The as-prepared $LiGaO_2$ electrodes were tested as positive electrodes against Li metal using a glass fiber separator (Whatman GF/D) and a polypropylene separator saturated with 1 M $LiPF_6$ in an ethylene carbonate and dimethyl carbonate (vol 1:1) electrolyte (LP30, battery grade, Sigma-Aldrich). The cells were assembled in Swagelok cells. Each cycling protocol started with a 20 h open circuit voltage (OCV). Afterward, cyclic voltammetry (CV) and galvanostatic charge/discharge experiments were carried out. The CV was recorded with a scanning rate of 0.02 mV s^{-1}. Three different potential ranges are applied in the CV: 0.6−4.2 V vs Li/Li^+, 0.05−3 V vs Li/Li^+, and 0.05−4.5 V vs Li/Li^+. At the upper and lower cutoff potentials, the potential was held for 20 h each. The same CV protocol was applied to initialize and monitor each cell for one cycle before the cells were measured through galvanostatic charge−discharge. The galvanostatic charge/discharge tests were performed at a current density of 10 mA g^{-1} in a potential range from 0.05 to 4.5 V vs Li/Li^+. At the respective cutoff potential, the potential was held for another 20 h for constant potential charge and discharge, respectively. To monitor the cell's equilibrium state afterwards, OCV was applied for 20 h before the next charge or discharge started. At least 7 cycles were recorded.

To prepare samples for the *ex situ* measurements, battery cells are assembled as described above and brought to the desired potential within the first CV cycle at a scanning rate of 0.02 mV/s. At each desired potential, a constant potential period of 20 h was applied, followed by an OCV period until the potential equilibrated. Table 1 gives an overview of the investigated *ex situ* samples: A-1 (for the OCV potential after equilibration of the just assembled cell), B-1 (4.5 V vs Li/Li^+), C-1 (0.05 V vs Li/Li^+), and D-1 (2.75 V vs Li/Li). Furthermore, *ex situ* samples were taken in the last (7th) cycle of the charge−discharge measurements at the upper and lower cutoff potential labeled as B-7 (4.5 V vs Li/Li^+) and C-7 (0.05 V vs Li/Li^+).

Table 1. Overview of the Investigated *Ex Situ* Points A-1, B-1, C-1, D-1 from the 1st CV Cycle, and B-7, C-7 from the 7th Cycle via Charge−Discharge

ex situ sample	condition	*ex situ* sample	condition
A-1	OCV before 1st cycle 2.75 V vs Li/Li		
B-1	after 1st charge to 4.5 V vs Li/Li^+	B-7	after 7th charge to 4.5 V vs Li/Li^+
C-1	after 1st discharge to 0.05 V vs Li/Li^+	C-7	after 7th discharge to 0.05 V vs Li/Li^+
D-1	1st cycle complete 2.75 V vs Li/Li		

X-Ray Powder Diffraction. X-Ray powder diffraction (XRPD) was used to measure the $LiGaO_2$ powder after synthesis and the cycled *ex situ* samples (A-1, B-1, C-1, D-1, B-7, and C-7). The $LiGaO_2$ powder sample was prepared by using the "front-load" method. A lab diffractometer (Empyrean, Panalytical) with a copper anode (Kα

https://doi.org/10.1021/acsami.4c03729
ACS Appl. Mater. Interfaces 2024, 16, 39181−39194

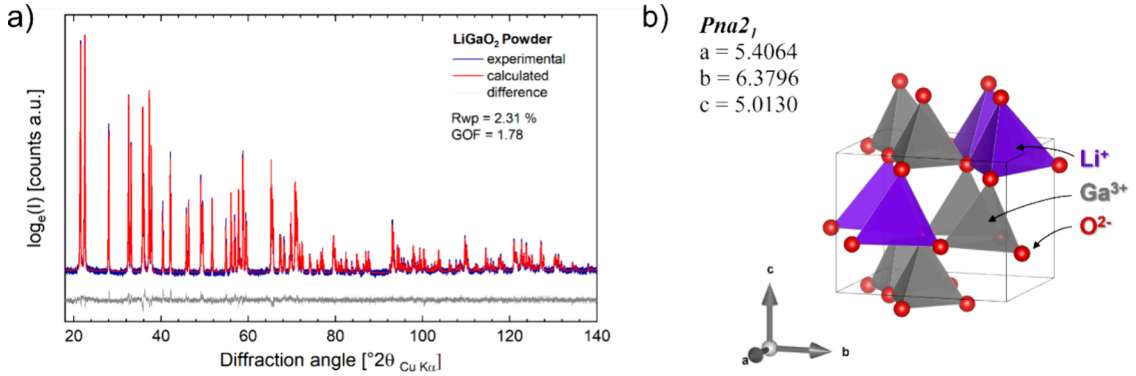

Figure 1. (a) Results of Rietveld refinement for XRPD of $LiGaO_2$: experimental XRPD data (blue), calculated data (red), and difference of $I_{obs} - I_{calc}$ (gray). Whole fitting range (17−140° 2θ) presented. (b) Visualization of the unit cell of $LiGaO_2$ in spacegroup $Pna2_1$.

Table 2. Refined Structural Parameters in Rietveld Refinement against Measured XRPD Data for the $LiGaO_2$ Powder Sample (see Figure 1)

$LiGaO_2$; $Pna2_1$; a = 5.406400(17), b = 6.37962(2), c = 5.013078(15); Rwp = 2.31%; GOF = 1.78						
Wyckoff position	atom type	fractional coordinate x	fractional coordinate y	fractional coordinate z	site occupancy	isotropic Debye−Waller factor (B_{iso}) [nm^2]
4a	Li	0.42070	0.1267	0.49360	1	0.612
4a	Ga	0.08261(9)	0.12541(8)	0.0	1	0.125(11)
4a	O	0.3974(4)	0.1430(8)	0.8876(3)	1	0.50(4)
4a	O	0.0628(4)	0.1105(9)	0.3633(3)	1	0.50(4)

wavelength: 1.54 Å) in reflection geometry was used to measure the $LiGaO_2$ pristine powder from 10 to 120°2θ, with a counting time of 30 s per step and a step size of 0.008°2θ. The *ex situ* samples were taken from the disassembled cells in a glovebox, mounted on Si substrates with Scotch Magic tape, and placed in a sample holder. The tape can be well penetrated by X-rays but protects the sample from direct contact with the atmosphere during the measurement.[25] A lab diffractometer (D8 Discover, Bruker) with a copper anode (Kα wavelength: 1.54 Å) in reflection geometry was used to measure the *ex situ* samples in an angular range from 10 to 120°2θ, with a counting time of 20 s per step and a step size of 0.02°2θ. Structural analysis and quantitative phase analysis (QPA) based on the XRPD data were carried out within the software package Diffrac.Topas (Bruker). The $LiGaO_2$ powder sample was structurally analyzed according to the Rietveld method.[26] The *ex situ* samples were analyzed by QPA from a full pattern fit of the XRPD data.[27]

Micro-Raman Spectroscopy. Micro-Raman spectroscopy was carried out with a WITEC alpha300R microscope using a solid-state 532 nm excitation laser and 600 L/mm grating with a laser power of 10 mW. The Raman spectra were collected with a 100× objective on an area of 80 μm × 80 μm and a 0.5 μm step raster for the pristine and *ex situ* samples of the first cycle. This yields 160 × 160 pixels, each containing an individual Raman spectrum. Due to the very low Raman activities and huge topography of the *ex situ* samples in the seventh cycle, the Raman analysis was carried out via volume mapping (by changing the stage height, i.e., focus point) in a volume of 50 μm × 50 μm × 50 μm with a 1 μm step size, yielding 50 × 50 × 50 pixels containing each one individual Raman spectrum. Each individual measurement at a point (pixel) was carried out with a 1 s acquisition time for both the volume and area mappings. The collected scans were treated by correction algorithms for cosmic ray removal, noise filtering, and baseline correction. Afterward, the data sets were analyzed through principal component analysis within the WITEC software package "WITEC project".

Scanning and Electron Microscopy and Energy-Dispersive X-Ray Spectroscopy. Both, top views (A-1, B-1, and C-1 and B-7) and cross-section analyses (B-7) were carried out to investigate the microstructure and elemental composition via scanning and electron microscopy (SEM) and energy-dispersive X-ray spectroscopy (EDX). The samples were consistently managed under vacuum or argon, and the Swagelok cell disassembly took place within an argon atmosphere inside a glovebox (MBraun and GS).

For top-view measurements, samples were investigated without further treatment, with the sample attached onto the SEM sample holder by carbon tape. For the cross-section preparation, the samples, including the Ni current collector, were divided into quarters using a Buehler IsoMet low-speed saw operating at a rotational speed of approximately 30 rpm. Subsequently, one of the quarters was ground using 3 M diamond sandpaper on a JEOL. A handy-lap grinder, starting with a grain size of 15 μm, progressing through 9, 3, 1, and 0.5 μm. Following this process, the ground surface underwent cross-sectional polishing in a JEOL IB-19530 CCP, utilizing an accelerating voltage of 4 kV. Active LN2 cooling to −100 °C was applied to prevent the temperature elevation of the sample. During the cross-sectional polishing, approximately 100 μm of the material was removed. The cross-section sample was affixed onto an SEM sample holder at a 90° angle, ensuring the polished side faced upward.

SEM images were collected on a Quanta FEG 650 FEI, USA, using an accelerating voltage of 5−20.0 kV with a secondary electron detector. Additionally, an FEI Helios NanoLab 460F1 FIB-SEM was used for a concentric back-scattered (CBS) image for the cross-sectional sample. For the EDX-analysis, an Ametek Octane Super at an accelerating voltage of 20 kV was employed on the top-view sample and an Ametek Octane Elite Super at an accelerating voltage of 5 kV for the cross-sectional sample.

X-Ray Photoelectron Spectroscopy and Electron Energy Loss Spectroscopy. Synchrotronic XPS measurement for $LiGaO_2$ at seventh cycle (charged state) and metallic Ga (as a reference) were performed in a 14A beamline of the Taiwan light source. Cryogenic electron energy loss spectroscopy (Cryo-EELS) measurements were conducted using an FEI Titan G2 ChemiSTEM 80−200 transmission electron microscope (TEM) equipped with a high-brightness field emission gun and probe spherical aberration (Cs) correction system operated at 200 kV. To mitigate electron beam damage, the sample was characterized by using a cryo-transfer holder (Simple Origin, Model 200). The EEL spectra were acquired in scanning transmission electron microscopy (STEM) mode with an annular dark-field (ADF) detector. The convergence semiangle was ∼25 mrad.

https://doi.org/10.1021/acsami.4c03729
ACS Appl. Mater. Interfaces 2024, 16, 39181−39194

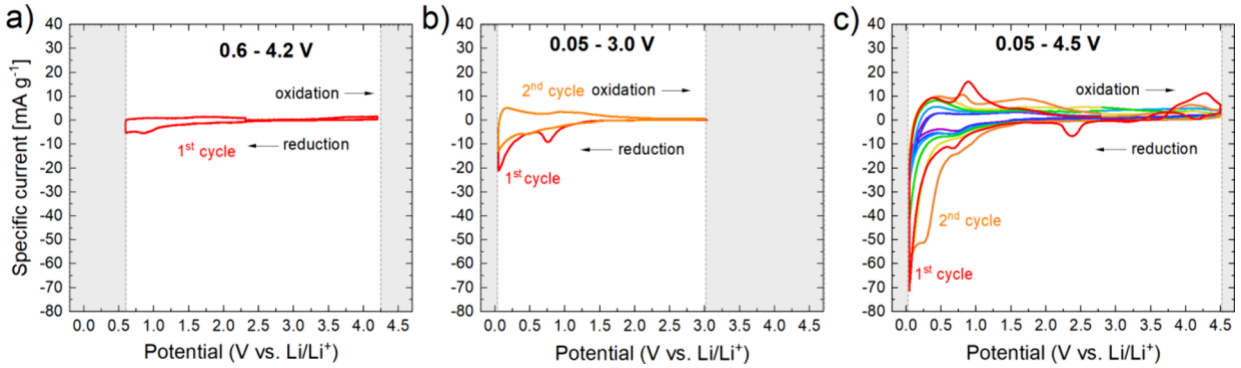

Figure 2. Cyclic voltammetry of $LiGaO_2$ against Li metal in an electrochemical test cell for (a) potential window 0.6−4.2 V vs Li/Li^+; (b) potential window 0.05−3.0 V vs Li/Li^+; and (c) potential window 0.05−4.5 V vs Li/Li^+.

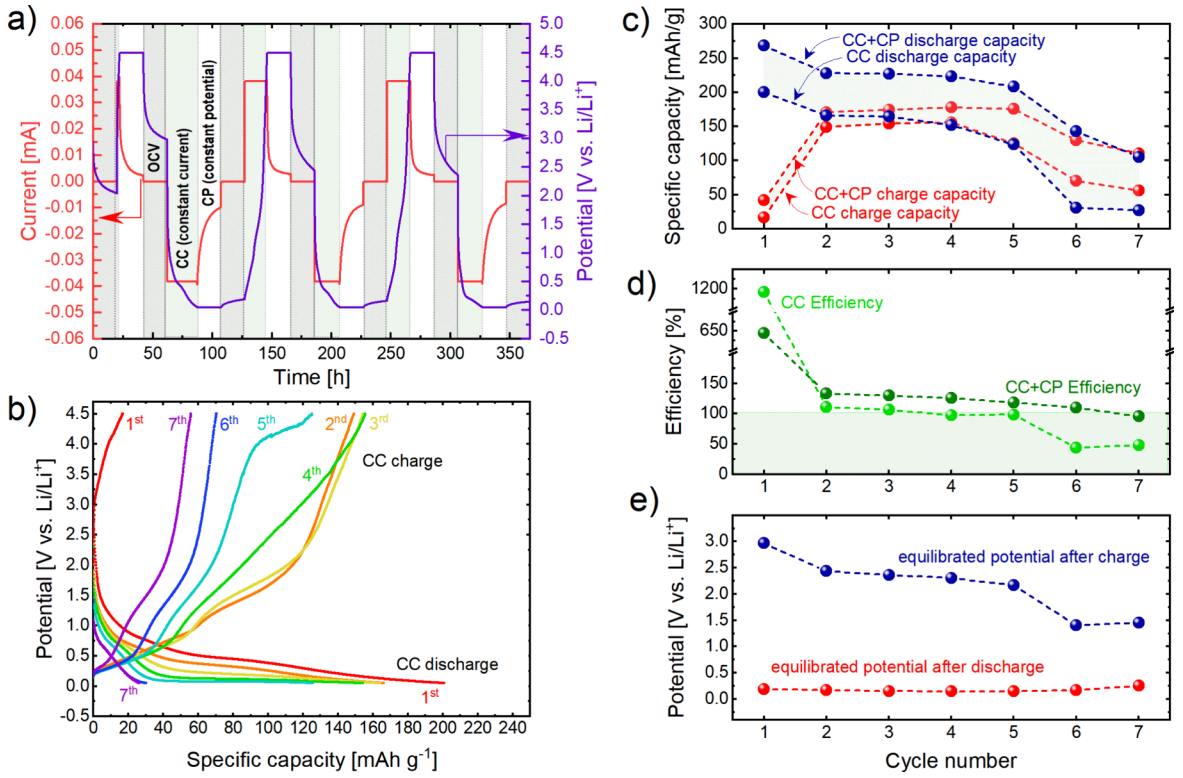

Figure 3. Results of the constant current (CC) + constant potential (CP) charge and discharge of $LiGaO_2$ against Li metal in an electrochemical test cell. (a) Cycling protocol with indicated OCV, CC, and CP periods; (b) potentials over capacities achieved with CC charge/discharge for the 1st to the 7th cycle; (c) achieved CC capacities in comparison to achieved CC + CP capacities as a function of cycle number; (d) efficiency as discharge capacity divided by charge capacity for CC and CC+CP as a function of cycle number; and (e) potential after each 20 h OCV period ("equilibrated" potential) as a function of cycle number.

RESULTS AND DISCUSSION

Structural Characterization of $LiGaO_2$ Powder. Figure 1 presents the X-ray powder diffraction pattern of the synthesized $LiGaO_2$. The observed Bragg peaks can be assigned to a reference structure of β-$LiGaO_2$ in space group $Pna2_1$ (ICSD coll. code 18152).[20] This phase was also used as a starting model in the following Rietveld analysis. The fit was carried out considering the $LiGaO_2$ scale factor, sample displacement, size, and strain broadening and through refining all relevant structural parameters, such as lattice parameters, Debye−Waller factors, fractional coordinates, and occupancies. All structural parameters (except Li fractional coordinates and Li isotropic Debye−Waller factors) were freed to converge. Their final results are given in Table 2. The lattice parameters only slightly deviate from the model structure (deviation less than 0.1%), and fractional coordinates only slightly shift compared to the model structure (shift less than 2%). There are no secondary phases visible in the pattern. Hence, our synthesis produced phase pure β-$LiGaO_2$ via solid-state reaction at 1200 °C in the space group $Pna2_1$. We are thus reporting the identical compound of $LiGaO_2$ in space group $Pna2_1$, which has been reported in the literature and has been extensively studied for its crystal structure,[20,28] band structure,[29,30] application as a substrate for GaN thin film deposition,[18,19,31] and employment as a dielectric ceramic.[32]

Furthermore, the synthesized $LiGaO_2$ polymorph is expected to be identical to the $LiGaO_2$ secondary phases in the Ga:LLZ system that have been reported in the

https://doi.org/10.1021/acsami.4c03729
ACS Appl. Mater. Interfaces 2024, 16, 39181−39194

literature.[7,9,10] It is known that, besides the polymorph in spacegroup $Pna2_1$, three other polymorphs exist for $LiGaO_2$. These polymorphs crystallize in either the α-$NaFeO_2$ structure type (spacegroup $R\bar{3}m$),[33] the NaCl structure type (spacegroup $Fm\bar{3}m$),[22] or in the β-$LiFeO_2$ structure type (spacegroup $I4/m$).[22] In the literature, the $LiGaO_2$ secondary phases were mostly identified from the main characteristic feature at 21−23°2θ in XRPD. Only $LiGaO_2$ in spacegroup $Pna2_1$ possesses this characteristic feature, due to its two main reflections 1 1 0 and 0 1 1 at 21.66 and 22.38°2θ, respectively. The other reported polymorphs are either high-pressure phases or metastable and thus unlikely to be formed during the reaction of Ga:LLZ at high temperature (>950 °C) and ambient pressure.[7,9,10] Thus, we expect that the herein reported $LiGaO_2$ polymorph in space group $Pna2_1$ is the very same polymorph that has frequently been reported to coexist as a secondary phase with Ga:LLZ garnet.[7,9,10]

Electrochemical Analysis of $LiGaO_2$ Electrodes. The as-synthesized $LiGaO_2$ powder was processed into electrodes by a typical procedure to be tested against Li metal in a laboratory cell.[34,35] Prior to each CV scan, the cells were set to the OCV for 20 h to reach their equilibrium potential between 2.3 and 2.5 V vs Li/Li^+. Figure 2 displays the results of the electrochemical activities during the CV scans in different electrochemical potential windows. In the first tested electrochemical potential window (Figure 2a), from 0.6 to 4.2 V vs Li/Li^+, a small nonreversible reduction reaction was observed at ∼0.8 V vs Li/Li^+. In the second tested electrochemical potential window (Figure 2b), from 0.05 to 3.0 V vs Li/Li^+, the CV scan discloses a more significant activity in the lower electrochemical potential region below 0.6 V vs Li/Li^+, peaking −20 mA g^{-1} upon reduction at 0.05 V vs Li/Li^+. The reaction shows reversibility but degrades quickly. The third tested electrochemical potential window is also the widest window tested, reaching from 0.05 to 4.5 V vs Li/Li^+ (Figure 2c). The CV records additional activities above 3.0 V vs Li/Li^+ upon oxidation and a dramatically increased activity below 1 V vs Li/Li^+, peaking at −70 mA g^{-1} in the first cycle upon reduction. The reactions display reversibility, although incomplete, as can be seen from the absence of symmetries in the oxidation and reduction curves. A large degradation of activity is observed upon cycling, leading to a fade of the peak current at 0.05 V vs Li/Li^+ during reduction to less than −10 mA g^{-1} in the seventh cycle.

The results demonstrate that the activity of $LiGaO_2$ strongly depends on the choice of the lower and upper cutoff potential. The recorded activities above 3 V vs Li/Li^+ may be critical for the access of the full activity in the low potential region, as can be concluded from the comparison of cycling to 3.0 and 4.5 V (Figure 2b,c). The displayed behavior in the CV gives a strong hint that a combination of high-voltage decomposition (or activation) and subsequent reversible reactions lead to a significant electrochemical activity through $LiGaO_2$ decomposition products in the potential window from 0.05 to 1.0 V vs Li/Li^+.

To investigate the electrochemical behavior deeper, a dedicated charge−discharge cycling protocol was applied to freshly prepared cells. The cycling protocol applied an initial OCV and 1 CV cycle followed by constant current (CC) and constant potential (CP) charge and discharge in the potential range from 0.05 to 4.5 V vs Li/Li^+ (Figure 3a). After each CC and CP dis/charge, an OCV of 20 h was applied to allow for the potential equilibration. Figure 3b demonstrates the achieved CC capacities and voltage profiles over 7 cycles. Like the CV results, the reaction activity is mostly concentrated at lower potentials <1.5 V vs Li/Li^+. Also, a reversible reaction is demonstrated over several cycles, with significant degradation of the achieved CC capacities.

Figure 3c displays the achieved CC charge and discharge capacities over cycle number and compares them with the achieved CC+CP discharge capacities over cycle number. It is obvious that applying a CP step after the CC steps yields 25−55 mAh g^{-1} additional charge capacity and 70−115 mAh g^{-1} additional discharge capacities. In the first cycle, a CC+CP charge capacity of 42 mAh g^{-1} is recorded, followed by a discharge capacity of 269 mAh g^{-1} and a second charge capacity of 172 mAh g^{-1}. In the seventh cycle, 109 and 106 mAh g^{-1} are recorded upon charge and discharge, respectively. In general, the CP charge and discharge capacities tend to get larger with a higher cycle number, while the CC+CP charge capacities first rise and then fade, whereas the discharge capacities show a steady fade. The corresponding efficiencies as a function of the cycle number are displayed in Figure 3d. Very large CC and CC+CP efficiencies are recorded for the first cycle: the discharge capacities are 1195% (CC) and 640% (CC+CP) higher than the charge capacities in the first cycle. In the second cycle, they fall to 111% (CC) and 136% (CC+CP) and fade slowly to 51% (CC) and 97% (CC+CP) in the seventh cycle.

If all Li can be extracted from $LiGaO_2$ during charging, then it would have a theoretical capacity of 247 mAh g^{-1}. The first charge capacity (42 mAh g^{-1}) thus suggests that up to 17% of the total amount of Li in the $LiGaO_2$ electrode has been extracted and transported to the negative electrode upon releasing one electron per extracted Li into the outer circuit during the CC+CP charge. As indicated by the high discharge capacity of the first cycle (269 mAh g^{-1}), 640% more Li is brought back into the positive electrode during the following discharge than was taken out during charge. This is only possible if a reaction product with a high Li storage capacity has formed upon charging in the first cycle. In the further cycles, this compound may undergo reversible electrochemical reactions with Li, as can be concluded from the reversible nature of the displayed activities in CV and galvanostatic charge−discharge cycling. Furthermore, the decomposition of $LiGaO_2$ into materials that allow to reversibly react to high amount of Li seems to be ongoing, at least until the sixth cycle, because of the recorded efficiencies above 100%.

During each OCV period between CC+CP charge and discharge, the evolution of the cell potential was recorded for20 h. As can be seen in Figure 3a, there is a significant potential drop in each OCV period after charging to 4.5 V vs Li/Li^+ and a noticeable potential rise during each OCV period after discharging to 0.05 V vs Li/Li^+. After the first charge, the potential falls from 4.5 to 2.9 V vs Li/Li^+ during 20 h of the OCV period. The potential after this 20 h OCV does not reach the equilibrium potential yet, as an asymptotic behavior of the potential-overtime function is not yet displayed. After the first discharge, the potential value rises from 0.05 to 0.2 V vs Li/Li^+ during 20 h of OCV. Here, an asymptotic behavior is displayed, and the cell seems to be in equilibrium. Figure 3e displays the (pseudo) equilibrated potential values at the end of each OCV period. As can be seen, the potentials after discharge rise slightly after the individual cycle, from 0.20 to 0.24 V vs Li/Li^+. On the other hand, the recorded potentials at the end of a 20 h OCV after charge show a continuous

https://doi.org/10.1021/acsami.4c03729
ACS Appl. Mater. Interfaces 2024, 16, 39181−39194

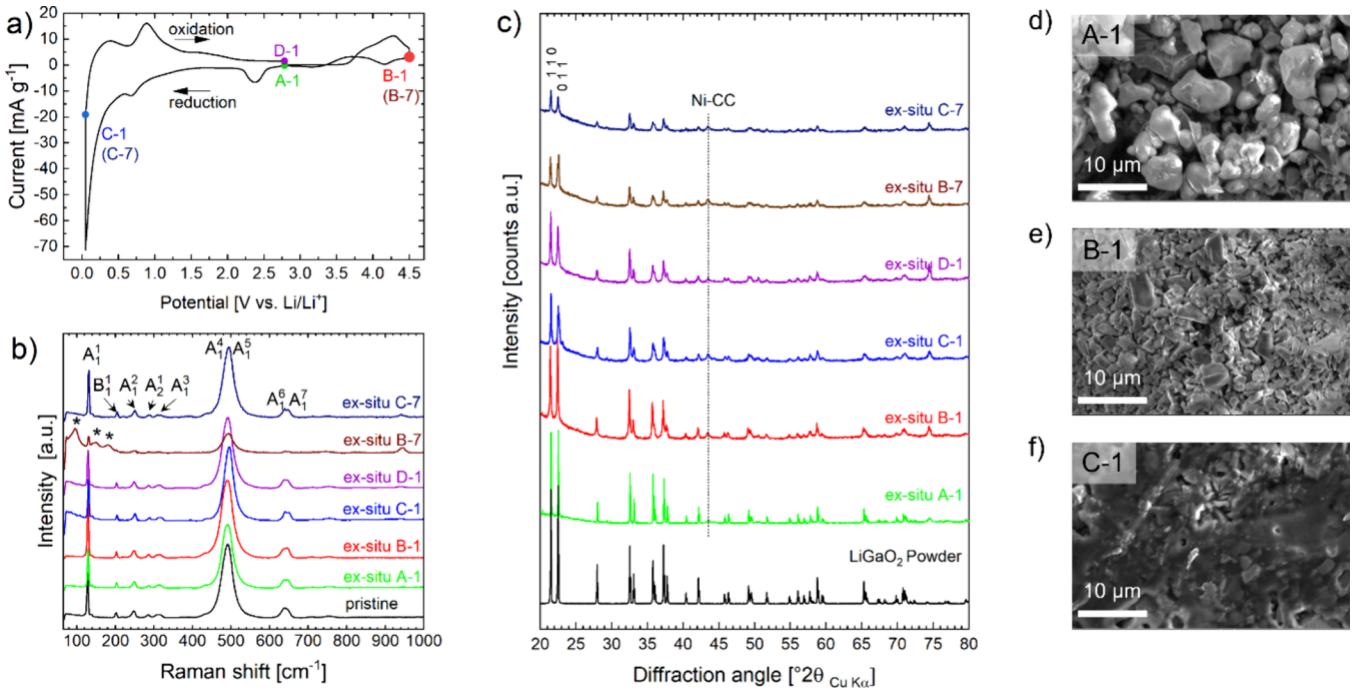

Figure 4. *Ex situ* analyses of the cycled $LiGaO_2$ electrode. (a) Indication of investigated *ex situ* points A-1, B-1, C-1, D-1 from the 1st CV cycle, B-7 and C-7 from the 7th cycle via charge−discharge. Reflections of the Ni current collector (Ni-CC) substrate are indicated by a dashed line; (b) averaged micro-Raman spectra from mapping areas of 80 × 80 μm (pristine electrode, A-1, B-1; C-1, D-1) and 50 × 50 μm (B-7, C-7) on current collectors; (c) XRPD data of the $LiGaO_2$ powder sample and A-1 to B-7 electrode samples on Ni-CC. (d−f) SEM images through secondary electron detection for A-1 (d), B-1 (e), and C-1 (f).

decrease over cycle number from 2.9 V vs Li/Li^+ to 1.45 V vs Li/Li^+.

The potential equilibrations to higher and lower potentials during an OCV period after charge and discharge, respectively, are typical for electrochemical cells due to polarizations and diffusion limitations. The potential will naturally equilibrate with the specific electrode potential of the material at the specific state of charge. Slower reaction kinetics during charge or discharge will usually lead to a stronger potential drop during OCV. The potential rise from 0.05 to 0.2 V vs Li/Li^+ in the OCV period after the first discharging thus suggests that the reaction has not been completed and a compound with an electrochemical potential of 0.2 V vs Li/Li^+ is formed. Most likely, the reaction would have kept going, if a smaller discharge current and a longer CP period had been applied. This is also supported by the observed decrease of the current during the CP period, which does not show full completion of the asymptotic trend yet after 20 h. This means the compound that we observe at the end of discharge is only partially electrochemically reacted, which is important information for interpretation of the later *ex situ* experiments. Furthermore, the slight rise in electrochemical potential during the individual OCV periods after each discharge suggests that the reaction kinetics worsen during cycling, meaning that compounds with different discharge states are produced at the end of each discharge cycle.

The potential drop in the OCV period after charging is significant and implies an additional underlying mechanism in addition to limited reaction kinetics. After the first charge, the potential during OCV drops back to a value the same as the pristine cell (2.95 V vs Li/Li^+), even though a significant capacity had been recorded. The dominant mechanism here seems to be the decomposition of $LiGaO_2$ above 4 V vs Li/Li^+. Obviously, the decomposition product must have a lower electrochemical potential than $LiGaO_2$, which is why the cell tends to equilibrate back to the electrochemical potential of $LiGaO_2$ during the OCV periods after discharge (which has the highest electrochemical potential in the formed composite material). Interestingly, the recorded potentials at the end of each OCV period decrease to 2.1 V vs Li/Li^+ in the fifth cycle and then drop to 1.41 and 1.45 V vs Li/Li^+ in the sixth and seventh cycles. The significant drop of the level of OCV means that $LiGaO_2$ must have either completely reacted into a different compound or has been isolated within the electrochemical cell in the sixth and seventh cycles, i.e., through microstructural degradation and loss of contact between $LiGaO_2$ and the reactions products, binders, and carbon.

Even though significant capacity degradation was observed, the underlying reversible nature in the following cycles strongly suggests that the formed product is a compound with a high reversible capacity in the lower potential range <1.5 V vs Li/Li^+. The electrochemical characteristics show striking similarities to the electrochemical reaction of Ga_2O_3 vs Li/Li^+.[36−38] In these studies, Ga_2O_3 is intentionally decomposed to Ga metal to form Li−Ga alloy electrodes.[36−38]

Structural and Microstructural *Ex Situ* Analyses. To further understand the electrochemical reactions of $LiGaO_2$, *ex situ* analyses via SEM, XRPD, and micro-Raman spectroscopy were carried out. Figure 4a indicates the measured voltages of the *ex situ* samples, which are also listed in Table 1. A-1 was taken after the initial OCV for potential equilibration, which has an equilibrated potential of 2.0 V vs Li/Li^+. B-1 was taken after oxidation through CV scan to 4.5 V vs Li/Li^+ and then set to OCV for 20 h. The final equilibrated potential of the cell was 3.0 V vs Li/Li^+. C-1 was taken after oxidation to 4.5 V and reduction to 0.05 V vs Li/Li^+ and resting at 0.05 V vs Li/Li^+

https://doi.org/10.1021/acsami.4c03729
ACS Appl. Mater. Interfaces 2024, 16, 39181−39194

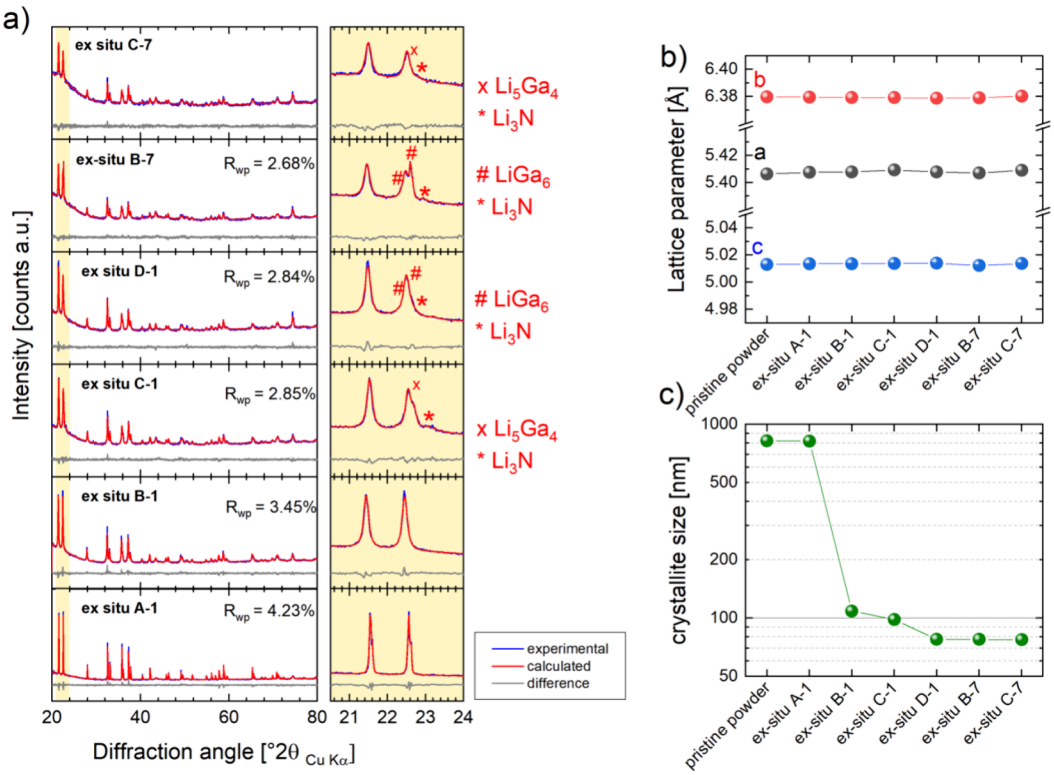

Figure 5. Results of the QPA based on XRPD data of the *ex situ* samples A-1 to C-7 (a) experimental, calculated, and difference for the fits in the fitting ranges 17−80°2θ; (b) evolution of refined $LiGaO_2$ lattice parameters over the sample series; and (c) evolution of refined crystallite sizes of the sample series.

for 20 h. It has an equilibrated potential of 0.22 V vs Li/Li^+. D-1 is taken after one full cycle plus rest (oxidation to 4.5 V and reduction to 0.05 V vs Li/Li^+ and another oxidation to 2.75 V vs Li/Li^+ and resting at 3.0 V vs Li/Li+ for 20 h). It has an equilibrated potential of 2.5 V vs Li/Li^+. B-7 is taken at the position of B-1 but after 7 additional cycles of charge−discharge. It has an equilibrated potential of 1.5 V vs Li/Li^+. C-7 is taken at the position of C-1 but after 7 additional cycles of charge−discharge. It has an equilibrated potential of 0.25 V vs Li/Li^+.

The results from Raman microscopy are shown in Figure 4b. Interestingly, the averaged Raman spectra all show the very same features and not much deviation from each other. As such, the recorded spectra for the pristine sample but also all the *ex situ* samples agree well with the Raman spectrum of β-$LiGaO_2$. β-$LiGaO_2$ has point group C_{2v} with experimental confirmed bands at 128.7 cm^{-1} ($A_1^{(1)}$), 204.2 cm^{-1} ($B_1^{(1)}$), 252.1 cm^{-1} ($A_1^{(2)}$), 289 cm^{-1} ($A_2^{(1)}$), 444.3 cm^{-1} ($A_1^{(3)}$), 493.3 cm^{-1} ($A_1^{(4)}$), 502.1 cm^{-1} ($A_1^{(5)}$), 643.9 cm^{-1} ($A_1^{(6)}$), and 653.8 cm^{-1} ($A_1^{(7)}$).[28,39] Accordingly, the Raman spectra for the pristine sample and *ex situ* A-1, B-1; C-1, D-1, and C-7 were indexed to the bands of β-$LiGaO_2$ in point group C_{2v}. Only the spectrum for the B-7 sample cannot be assigned to β-$LiGaO_2$ alone. Here, the bands from the β-$LiGaO_2$ modes seem to have vanished while new, weak, and broad bands emerged at 99, 145, and 182 cm^{-1} (indicated by * in Figure 4b), which will be discussed in more detail later.

Similarly, the XRPD patterns (Figure 4c) show $LiGaO_2$ in $Pna2_1$, as the main phase in all *ex situ* samples, resembling the pristine powder. There are changes in the intensity ratios of the two main reflections, and shoulders emerge predominantly at the *0 1 1* reflection at 22.6° (Figure S1 in the Supporting Information provides a more detailed view). Further, it is noted that the reflection maximum intensities get weaker, and the Bragg peaks tend to broaden throughout the sample series. The peak broadening suggests a significant change in a microstructure, i.e., crystallite sizes or strains of $LiGaO_2$ crystallites. At this stage, it must be assumed that any possible decomposition products are hard to detect through Raman spectroscopy and XRPD where their only evidence may lay in the subtle changes in the spectra (e.g., *ex situ* sample B-7) and their diffraction patterns (e.g., intensity ratios and peak shoulders in B-1 to C-7).

As the Bragg peak broadening is the most obvious from samples A-1 to B-1, electron microscopy was used as a complementary tool for understanding the underlaying mechanism. A drastic change in the microstructure was observed in the SEM images for the sample A-1 to the sample B-1 (Figure 4d,e) where sample A-1 shows $LiGaO_2$ particles with a size distribution from 1 to 10 μm, with most of the particles in between 7 and 10 μm and sample B-2 on the other hand shows smaller particle distribution between 1 and 5 μm and only a few particles above 7 μm. These results suggest that, even though $LiGaO_2$ seems to be majorly preserved in the *ex situ* samples, it does undergo a significant microstructural change. For sample C-1 (Figure 4f), a new microstructural feature is present, which has the appearance similar to a melt. Similarly, optical images taken for all *ex situ* samples show a drastic changing microstructure from a pure powder-like sample to a solidified specimen under the presence of a melt phase (see Figure S2, Supporting Information).

Quantitative Phase Analysis from XRPD. The possible presence of Li−Ga alloys or Ga was further analyzed through quantitative phase analysis based on the collected XRPD data.

https://doi.org/10.1021/acsami.4c03729
ACS Appl. Mater. Interfaces 2024, 16, 39181−39194

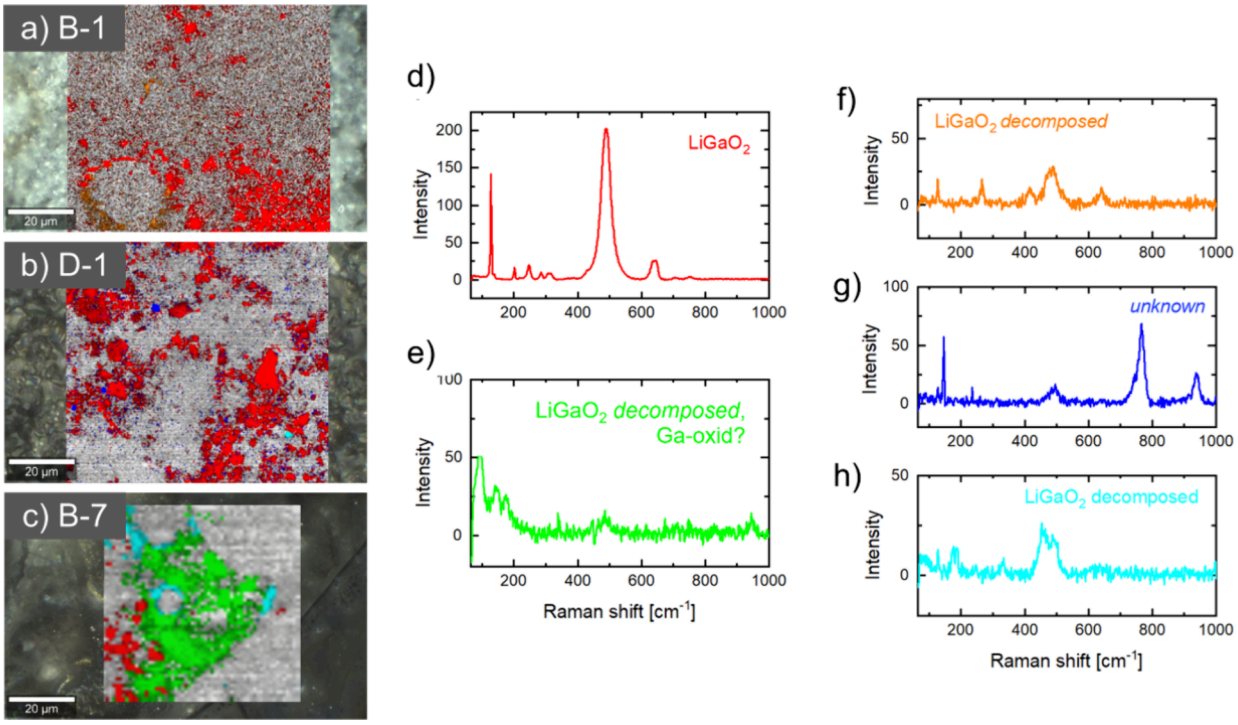

Figure 6. Results of principal component analysis from micro-Raman mappings for the samples (a) B-1 (first charge to 4.5 V vs Li/Li^+), (b) D-1 (first full cycle), and (c) B-7 after charging to 4.5 V vs Li/Li^+ in the 7th cycle. Each color represents an identified individual component through the principal component algorithm. Gray areas are out of focus or have intensities that are too low. For each component, a representative individual spectrum is shown: (d) $LiGaO_2$, (e) decomposed $LiGaO_2$ or Ga-oxide, (f) low intensity area/decomposed $LiGaO_2$, (g) unassigned, and (h) low intensity area/decomposed $LiGaO_2$.

In parallel, the $LiGaO_2$ phase was quantified with respect to its lattice parameters and crystallite sizes to understand its contribution to the reactions during cycling. To describe the main $LiGaO_2$ phase in the diffractograms, the refined structural parameters of the $LiGaO_2$ powder sample (Figure 1, Table 2) were used as the starting values. Parameters like the fractional coordinates, Debye−Waller factors, and site occupancies were kept fixed at their refined values from the $LiGaO_2$ powder sample, while lattice parameters, sizes, and strains were refined against the measured data. Besides $LiGaO_2$ and Ni (as the CC), possible impurity phases such as Li_3N, Li_2O, LiOH, $LiOH{\cdot}H_2O$, and Li_2CO_3 and a series of possible reaction products such as Ga_2O_3, $LiGa_5O_8$, Li_5GaO_4 as well as various Li−Ga alloys, and Ga metal were testes within the quantitative phase analysis routine. It was concluded that none of the above-mentioned phases could be fitted reasonably against the measured data besides Ni, Li_3N, and some specific compositions of a Li−Ga alloy. Structural information files for these samples were taken from ICSD references as listed in Table S1, Supporting Information.[20,40−43]

Figure 5a shows the fitting results of QPA for the sample series. The evolution of the refined lattice parameters and crystallite sizes is shown in Figure 5b,c. For comparison, the refined lattice parameters and crystallite size for the pristine $LiGaO_2$ powder sample are shown, too. As can be seen, the refined values for the lattice parameters remain constant throughout the sample series, while the crystallite sizes show a clear decreasing trend upon cycling. The crystallite size for the *ex situ* A-1 (OCV equilibrated) sample refines to a similar value (820 nm) than the refined crystallite size for the pristine powder sample (823 nm). For the B-1 sample, the crystallite size refined significantly smaller to 108 nm. Over the sample series, this value steadily decreases and refined to 77 nm for C-7.

The XRD patterns for C-1, D-1, B-7 and C-7 cannot be described from the contribution of a $LiGaO_2$ phase alone. A small fraction of Li_3N contaminations must be considered, which most likely arises from reactions with the ambient atmosphere. Even though the sample was protected from the atmosphere by the Scotch magic tape, these reactions can happen if highly reactive phases (such as Li or Li−Ga alloys) are present in the sample. Neither Ga_2O_3 nor Li−Ga−O related phases, such as $LiGa_5O_8$ or Li_5GaO_4 could be fitted against the measured data. Still, C-1, D-1, B-7, and C-7 remained poorly described by considering only $LiGaO_2$ and Li_3N. This is especially evident from the region between 21 and 22°2θ, where shoulders and peaks next to the main reflection of $LiGaO_2$ emerge (see Figure 5a, enlarged region).

For *ex situ* C-1 and C-7, the main reflection of Li_5Ga agrees with the position of the shoulder at 22.5°2θ. However, considering its contribution to the diffraction pattern of the C-1 sample, is successful only if a high texture for its *0 0 l* reflection is considered. Similarly, $LiGa_6$ can be fitted against the measured data for D-1 and B-7 and successfully describe the shoulders and peaks and 22.0−22.5°2θ, if a strong texture for its *0 0 l* reflections is considered. While this may indicate the presence of Li−Ga alloys in the sample, it cannot completely exclude the presence of Ga, Ga_2O_3, or Li−Ga−O ternary compounds in the samples. Ga metal, which has a melting point at 29.77 °C, is most likely in the liquid state or a supercooled liquid and thus X-ray amorphous. On the other hand, Li−Ga-oxides or Ga_2O_3, if decomposed from $LiGaO_2$ at higher voltage, are unlikely to show a good crystallinity. They may present as a low-crystalline or nanoscale secondary phase

https://doi.org/10.1021/acsami.4c03729
ACS Appl. Mater. Interfaces 2024, 16, 39181−39194

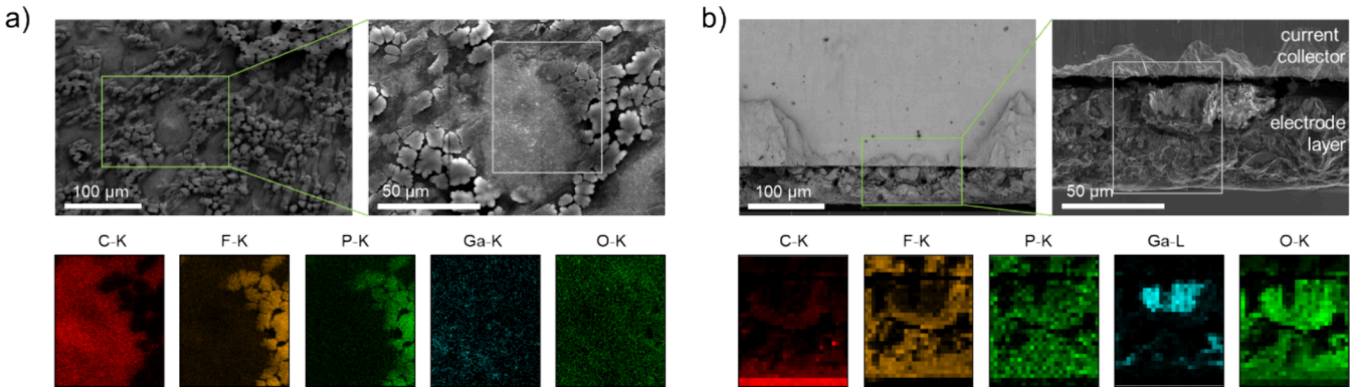

Figure 7. SEM and correlative EDX mappings for (a) top view of the B-7 sample (left accelerating voltage 5 kV, right accelerating voltage 20 kV) and (b) cross section of the B-7 sample (accelerating voltage 5 kV).

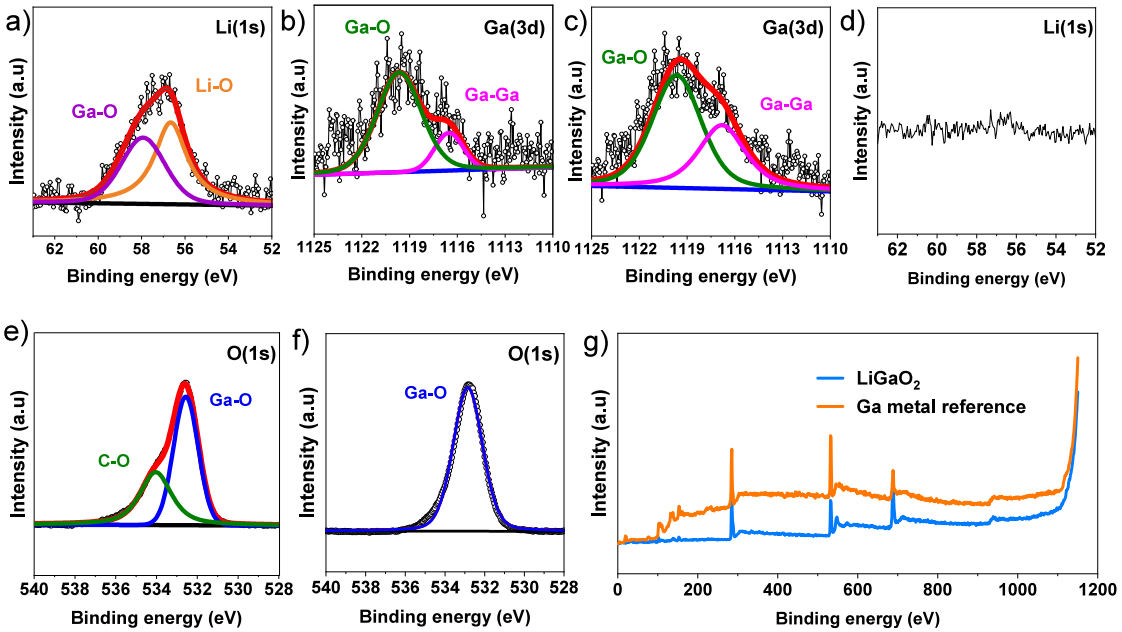

Figure 8. XPS spectra for the B-7 sample and metallic Ga reference sample. Panels a and b are Li(1s) and Ga(3d) spectra for the B-7 sample; panels c and d are Ga(3d) and Li(1s) spectra for metallic Ga samples. Panels e and f are spectra belong to O(2s) for B-7 and metallic Ga, respectively. (g) XPS survey for both B-7 and metallic Ga samples.

that cannot readily be identified in the given diffraction patterns.

Component Analyses from Micro-Raman Spectroscopy Mapping. To investigate possible reaction products in the system further, the collected micro-Raman maps for the samples B-1 (1st charge), D-1 (1st full cycle), and B-7 (7th charge) were analyzed through a principal component algorithm within the WITEC project software package. The results of the analysis are displayed in the color-coded maps in Figure 6a–c, and their representative individual spectra of the identified components are shown in Figure 6d–h. After the first charge and after the first full cycle, the main component in the mapped area was $LiGaO_2$ (Figure 6d), as was already represented by the averaged spectrum from the mapped area of the sample B-1 and D-1 in Figure 4b.

In the mapped area of the seventh charge to 4.5 V vs Li/Li^+, a new main component (Figure 6e) appears to be widely distributed over the mapped area. The component shares the feature of the averaged spectra of sample B-7 in Figure 4b, with a main, yet weak, band at 99 cm^{-1} and 2 more weak bands at 145 and 182 cm^{-1}. Compared to $LiGaO_2$, the newly identified component has a much lower Raman activity, as can be seen from the absolute intensity scales in Figure 6d,e. From the electrochemical analysis, where similarities with the Ga_2O_3 and Ga electrochemical activities vs Li were recorded, decomposition products such as gallium oxides or Ga metal may be expected. Gallium-oxide in the form of Ga_2O_3 is known to have many polymorphs each having their own individual Raman spectra.[44−47] Most of the experimentally recorded Raman spectra for Ga_2O_3 do not agree to the observed features for the identified component in Figure 6e. Similarly, not a single band matches the Ga-metal Raman spectrum.[48] The only similarities are identified for the κ/ε-Ga_2O_3 spectrum.[47] However, due to the low Raman activity and poor signal/noise, the assignment of bands is rather difficult. Besides, in the spectrum, we note that some features of the $LiGaO_2$ spectrum are still well preserved, like the $A_1^{(4)}$ and $A_1^{(5)}$ modes as the main feature in the $LiGaO_2$ spectrum at ~490 cm^{-1}. Furthermore, $LiGaO_2$ components with their characteristic spectra have been identified in some areas of the sample dominantly, as shown

https://doi.org/10.1021/acsami.4c03729
ACS Appl. Mater. Interfaces 2024, 16, 39181−39194

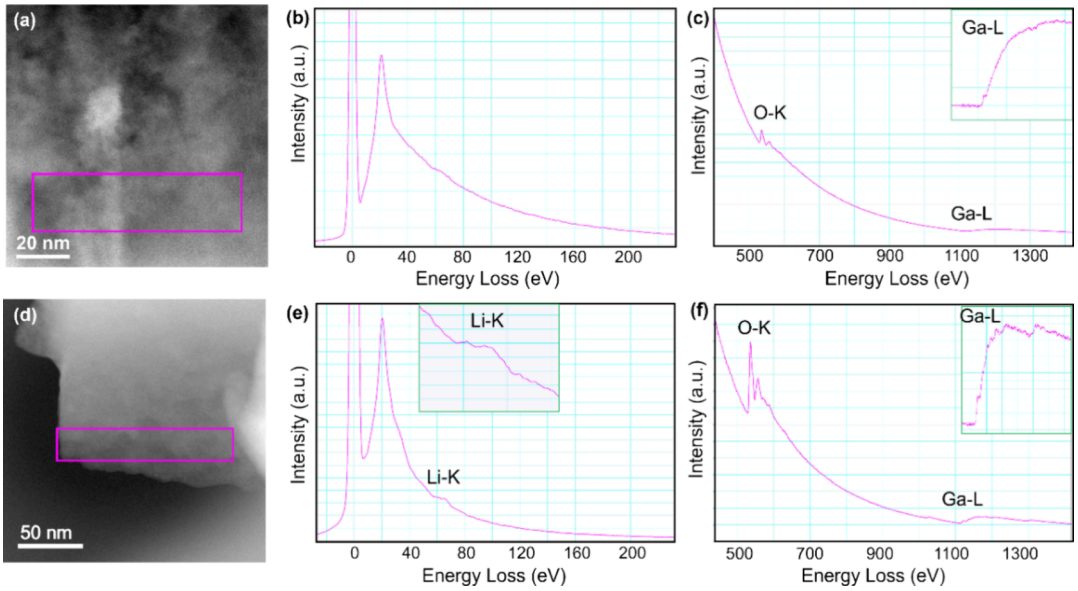

Figure 9. EELS spectra of the B-7 sample in different areas. (a) ADF-STEM image of the sample. (b) Low-loss EELS spectra, and (c) ionization edges corresponding to the O−K and Ga−L edges as indicated of selected area in panel a. The near-edge fine structure (ELNES) of Ga−L is enlarged (inset). (d) ADF-STEM image of the sample. (e) Low-loss spectra of the surface region, it shows the presence of Li. The ELNES of Li−K is enlarged (inset, f) corresponding O−K and Ga−L edges for the selected area as shown in panel d. The ELNES of the Ga−L peak is enlarged (inset).

by the red areas in the map of sample B-7. Three secondary components with a small distribution in the mapped area and a rather weak intensity compared to that of the collected $LiGaO_2$ spectrum were identified (Figure 6f−h). The results suggest that, even at the scale of micro-Raman spectroscopy (lateral resolution of 500 nm), single phases cannot be identified. Most likely, the sample is heavily inhomogeneous even at the upper nanoscale. Yet, the presence of Li−Ga alloys or liquid Ga cannot be excluded from being present in the sample because of their Raman inactivity.

Scanning Electron Microscopy and Energy-Dispersive X-Ray Spectroscopy. As a further step to identify the nature of the possible decomposition and reaction products, SEM and correlative EDX mappings were collected for the B-7 sample (Figure 7). In the top view of the sample, the binder in the electrode and carbon additive can still be clearly identified from its F−K and P−K signals. Carbon seems to be majorly present in the selected area, as evidenced from its C−K signal. However, Ga or O failed to be localized and showed only a weak and broad distribution throughout the investigated area.

The cross-section EDX map reveals a high concentration of C at the surface of the electrode sheet. F−K and P−K signals can be found throughout the electrode layer and indicate the presence of the used binder. Toward the current collector, the microstructure turns from a densified top layer into an agglomeration-like structure with obvious pores and microstructural disintegration of material from the rest of the layer. Yet, the gap between the layer and current collector may be an artifact from the cross-section polishing procedure. Ga can be localized in densified agglomerates, in addition to O and surrounded by an O-rich periphery, as evidenced by the Ga−L and O−K signals (Figure S3, Supporting Information, provides further EDX maps showing similar features on a different area of the sample). Interestingly, the areas where binder is present (F and P rich) show significant signals for the O−K, suggesting that the binder became heavily oxidized or new oxide products have been formed among the matrix.

X-Ray Photoelectron Spectroscopy and Electron Energy Loss Spectroscopy. Synchrotronic XPS measurement for $LiGaO_2$ at seventh cycle (charged state, B-7) and metallic Ga (as a reference) were performed in the 14A beamline of the Taiwan light source. For the $LiGaO_2$ sample (B-7), Li(1s) spectra indicate the presence of Li_2O and $LiGaO_2$ from Li−O at around 57 eV and possible Ga_2O_3/$LiGaO_2$ from Ga−O at 58.27 eV[49−51] as indicated in Figure 8a−c. However, in Figure 8d, there is no peak belonging to metallic Ga in Li 1s spectra, which was used as a reference. It is interesting to observe the peak ratio difference of Ga−O (1119.65 eV) to the metallic gallium (Ga−Ga) peak (1116.53 eV).[52,59] The Ga−Ga peak is comparably smaller in the B-7 sample than in the Ga reference; however, it indicates the presence of metallic gallium for the $LiGaO_2$ electrode in the charged state after the seventh cycle, which will be further discussed later.

Furthermore, the O(1s) spectra from Figure 8e for the $LiGaO_2$ sample shown two peaks associated with C−O (534.06 eV)[5] from the conductive carbon or electrolyte and Ga−O (532.56 eV) peak from the $LiGaO_2$ electrode sample, whereas the metallic Ga samples shown one intense peak at around 532.56 eV from Ga−O[52] as indicated in Figure 8f. Here, based on O(1s) spectra, it is hard to identify $LiGaO_2$ or Ga_2O_3 because of the similarity in their binding energy. The Li(1s) and Ga(3d) spectra can be used as solid evidence for the presence of $LiGaO_2$ in the B-7 sample, which agrees to our previous observations from PXRD, Raman, and electrochemical analyses where the presence of $LiGaO_2$ was confirmed too. The XPS survey for both $LiGaO_2$ and metallic Ga included for comparison purpose as demonstrated in Figure 8g.

Ga_2O_3 cannot be separated unambiguously from $LiGaO_2$ through XPS, due to the coexistence of $LiGaO_2$ and their

https://doi.org/10.1021/acsami.4c03729
ACS Appl. Mater. Interfaces 2024, 16, 39181−39194

similarities in Ga−O binding energies but could also not be separated from $LiGaO_2$ at the length scale of SEM/EDX. To probe an even smaller length scale and decouple $LiGaO_2$ form possible Ga_2O_3 signals, cryo-EELS measurements were conducted on the B-7 sample (charged to 4.5 V after the seventh cycle). A low-loss EELS spectrum from the bulk of this sample indicates the absence of Li in this area (Figure 9b). Figure 9c displays the O *K*-edge and Ga *L*-edge, enabling us to identify the composition of this region as Ga_2O_3,[53,54] thus proving Ga_2O_3 formation from $LiGaO_2$ decomposition above 3.5 V vs Li/Li^+. Furthermore, in the surface area, as shown in Figure 9d−f, $LiGaO_2$ was detected from its Li−K, O−K, and Ga−L signals. This proves the existence of Ga_2O_3 besides $LiGaO_2$ on a length scale of a few hundred nm.

Derived Reaction Mechanism for $LiGaO_2$ Electrochemical Activity. Based on our observations from electrochemical analysis and *ex situ* Raman, XRPD, SEM/EDX, STEM/EELS, and synchrotron XPS analyses, we derive the following reaction mechanism for the electrochemical activity of $LiGaO_2$ (Figure 10).

charge activation: >3.5 V vs Li/Li^+: $2LiGaO_2 \rightarrow 2Li^+ + Ga_2O_3 + {}^1/_2O_2 + 2e^-$ (1)

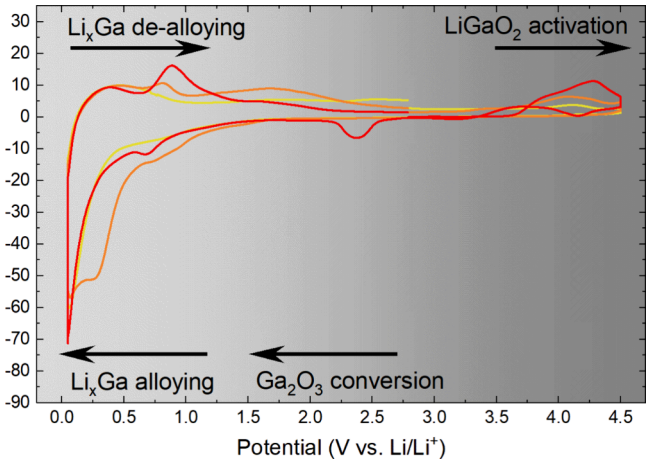

Figure 10. Overview of the identified reaction mechanism for $LiGaO_2$ from 0.05 to 4.5 V vs Li/Li^+.

The first cycle starts from the OCV at 2.75 V vs Li/Li^+. In the first charge, above 3.5 V versus Li/Li^+, $LiGaO_2$ is activated, meaning it starts to decompose. Li^+ transfer from the positive $LiGaO_2$ electrode to the negative Li-metal electrode is evident from the measured current. Here, Li^+ is released into the electrolyte to be combined with one electron at the negative electrode, which goes through an external circuit from the positive to negative electrode. The remaining compound in the $LiGaO_2$ electrode thus has to be oxidized to maintain the charge balance.

Ga as a group IIIA member can only have valence states as Ga^0 or Ga^{3+}. Formation of Ga^0 at high potentials would contradict its calculated thermodynamic stability (Pourbaix diagram, Figure S4).[55−58] Thus, Ga^{3+} is unlikely to change its valence state during the electrochemical oxidation reaction at high voltage, limiting the possible reaction product to Ga^{3+} containing oxide compounds. However, the formation of Li−Ga−O ternary compounds with a lower Li-stoichiometry than $LiGaO_2$, such as $LiGa_5O_8$, does not agree with thermodynamic considerations of the Li−Ga−O stabilities at high voltage either. In fact, the thermodynamic calculations strongly suggest that Ga_2O_3 is formed.[55−58] To form Ga_2O_3 from 2 $LiGaO_2$, 1/2 O_2 needs to be released to balance the reaction. This O_2 evolution reaction (OER) is instantaneously coupled to the decomposition of $LiGaO_2$ above 3.5 V vs Li/Li^+ and will readily oxidize the other compounds in the electrode. The proposed OER during reaction (1) agrees with our observations in SEM/EDX, where large oxidations in the region of the binder matrix was observed in the charged sample after 7 cycles and where areas with high concentration of Ga were surrounded by an O-rich periphery, while Ga itself could not be separated from O even at the length scale of SEM/EDX. Finally, STEM/EELS revealed that Ga_2O_3 is present in the sample besides $LiGaO_2$ at the nanometer length scale, thus unambiguously proving that $LiGaO_2$ decomposes to Ga_2O_3 at potentials above 3.5 V vs Li/Li^+, and Li being extracted electrochemically from the system.

discharge conversion reaction:

<2.5 V vs Li/Li^+: $Ga_2O_3 + 6Li^+ + 6e^- \rightarrow 2Ga + 3Li_2O$ (2)

reversible alloying reaction:

0.05 − 1.0 V vs Li/Li^+: $Ga + xLi^+ + xe^- \leftrightarrow Li_xGa$ (3)

During discharge, measurable activity is detected below 2.5 V vs Li/Li^+. The current increases steadily while going to lower potentials. Based on the previous observations for Ga_2O_3 formation in reaction 1, the reaction 2 during discharge is expected to arise from the Ga_2O_3 electrochemical conversion reaction, leading to metallic Ga and Li_2O. The conversion reaction of Ga_2O_3 is well-known in the literature and has been demonstrated to lead to subsequent reversible alloying reactions that take place between 0.0 and 1.0 V vs Li/Li^+.[36] This agrees to the observed reversibility of the electrochemical reaction in our experiments below 1.0 V vs Li/Li^+, for comparison see also Figure S5, Supporting Information.

The ideal electrochemical Li−Ga alloying reaction shows distinct electrochemical reactions at 0.14 V vs Li/Li^+ during discharge and 0.78 and 0.86 V vs Li/Li^+ during charge, Figure S6, Supporting Information. While striking differences can still be seen in terms of polarization and reversibility of the pure Li−Ga alloying reaction, the agreement with the alloying potential window of Li−Ga is obvious. Furthermore, our data agree very well with the Ga_2O_3 electrochemical activity,[36,37,47] in terms of shapes and reversibility of the observed CV curves (Figure S5, Supporting Information). Furthermore, the reaction product in reaction 3 is metallic Ga, which has been clearly identified to be present in the charged sample after 7 cycles via XPS, in addition to Ga_2O_3 and $LiGaO_2$.

The presence of $LiGaO_2$ in all *ex situ* samples, as evidenced by XRPD, Raman spectroscopy, XPS, and EELS implies that, for the chosen experimental setup, $LiGaO_2$ has not been fully activated during the recorded 7 cycles. This may be due to the rather large particle size of $LiGaO_2$ that limits the electrochemical reaction to the surface of the $LiGaO_2$ particles. Especially $LiGaO_2$ itself does not provide sufficient electronic conductivity to free up electrons upon decomposition of bulk $LiGaO_2$ in reaction 1. From the observed microstructural

https://doi.org/10.1021/acsami.4c03729
ACS Appl. Mater. Interfaces 2024, 16, 39181−39194

degradation through QPA based on the *ex situ* XRPD data, we can conclude that most of the activation of $LiGaO_2$ takes place in the first charge. During the first discharge, Ga_2O_3 conversion is the major reaction, while in the subsequent charge and discharge cycles, the Li−Ga alloying and dealloying dominate.

The decomposition of $LiGaO_2$ at electrochemical potentials >3.5 V vs Li/Li^+ and the subsequent electrochemical reactions suggest that the presence of $LiGaO_2$ at grain boundaries of Ga:LLZO electrolytes can subject full cell ASSLMB with Ga:LLZO electrolytes to short circuiting during cycling. In full cells, layered oxide positive electrodes (such as $LiCoO_2$ or $Li(Ni,Mn,Co)O_2$) are usually employed, which yield a cell potential of the ASSLMB at 4.2 V or higher.[1−3] Cycling these cells will easily decompose $LiGaO_2$ into Ga_2O_3. Since Ga_2O_3 has an electrochemical potential higher than metallic Li, Li^+ will preferably react to Ga_2O_3 to form Ga and Li_2O instead of reducing to Li metal at the negative electrode during the discharging process. Therefore, short circuiting of the ASSLMB will happen through the $LiGaO_2$ phase even without physical contact to the metallic Li at the negative electrode. The experimental results thus highlight the importance of eliminating $LiGaO_2$ formation at the grain boundaries of Ga:LLZO to realize its ASSLMB application.

CONCLUSIONS

The study reports the electrochemical activity of $LiGaO_2$, tested in a Li-ion type battery as positive electrode against Li metal as a negative electrode, with a Li^+ conducting liquid electrolyte. We could show that $LiGaO_2$ gets activated above 3.5 V vs Li/Li^+, by decomposing to Ga_2O_3 under OER and the extraction of Li^+ into the electrolyte, thus leading to the anodic reaction to Li metal at the negative electrode. The subsequent electrochemical reactions involve the reversible Li−Ga alloying and dealloying in the voltage range from 0.05 to 1 V vs Li/Li^+ with significant capacities of up to 200 mAh g^{-1}. The results have considerable implications for the use of full solid-state cells with Ga-doped garnet solid electrolytes, where $LiGaO_2$ is known to coexist with the garnet main phase. Especially for the cycling conditions in full cells, usually above 3 V vs Li/Li^+, $LiGaO_2$ is expected to be activated and electrochemically reacted into Li−Ga alloy phases. Those reaction products will subject the solid electrolyte to cell failures through short circuits. The results highlight the importance of the knowledge-based design of solid electrolytes to realize high-performance solid-state batteries.

ASSOCIATED CONTENT

Supporting Information

The Supporting Information is available free of charge at https://pubs.acs.org/doi/10.1021/acsami.4c03729.

Additional experimental results and references: close-up view for XRD for all compounds; optical microscopy images for all compounds; table with reference structures in the quantitative phase analysis; SEM/EDX at cross section, Pourbaix diagram of Li−Ga−O; and comparison of $LiGaO_2$ CV in this study with Ga_2O_3 CV from the literature, comparison of $LiGaO_2$ CV in this study with Ga-metal CV as a control sample (PDF)

AUTHOR INFORMATION

Corresponding Author

Anna Windmüller − *Institute of Energy Technologies (IET-1: Fundamental Electrochemistry), Forschungszentrum Jülich, Jülich 52425, Germany; Department of Chemical Engineering, Nano-electrochemistry Laboratory and Sustainable Electrochemical Energy Development Center, National Taiwan University of Science and Technology, Taipei City 106, Taiwan;* orcid.org/0000-0003-2829-3362; Phone: +49 2461 61-96867; Email: a.windmueller@fz-juelich.de

Authors

Kristian Schaps − *Institute of Energy Technologies (IET-1: Fundamental Electrochemistry), Forschungszentrum Jülich, Jülich 52425, Germany; Institute of Electrical Engineering and Information Technology, FH Aachen − University of Applied Sciences, Aachen 52066, Germany*

Frederik Zantis − *Institute of Energy Technologies (IET-1: Fundamental Electrochemistry), Forschungszentrum Jülich, Jülich 52425, Germany; Institute of Physical Chemistry (IPC), RWTH Aachen University, Aachen 52066, Germany*

Anna Domgans − *Institute of Energy Technologies (IET-1: Fundamental Electrochemistry), Forschungszentrum Jülich, Jülich 52425, Germany; Institute of Physical Chemistry (IPC), RWTH Aachen University, Aachen 52066, Germany*

Bereket Woldegbreal Taklu − *Department of Chemical Engineering, Nano-electrochemistry Laboratory and Sustainable Electrochemical Energy Development Center, National Taiwan University of Science and Technology, Taipei City 106, Taiwan;* orcid.org/0000-0002-8550-4835

Tingting Yang − *Ernst Ruska-Centre for Microscopy and Spectroscopy with Electrons (ER-C 1), Forschungszentrum Jülich GmbH, Jülich 52425, Germany*

Chih-Long Tsai − *Institute of Energy Technologies (IET-1: Fundamental Electrochemistry), Forschungszentrum Jülich, Jülich 52425, Germany;* orcid.org/0000-0001-8103-3514

Roland Schierholz − *Institute of Energy Technologies (IET-1: Fundamental Electrochemistry), Forschungszentrum Jülich, Jülich 52425, Germany;* orcid.org/0000-0002-2298-4405

Shicheng Yu − *Institute of Energy Technologies (IET-1: Fundamental Electrochemistry), Forschungszentrum Jülich, Jülich 52425, Germany;* orcid.org/0000-0002-6619-3330

Hans Kungl − *Institute of Energy Technologies (IET-1: Fundamental Electrochemistry), Forschungszentrum Jülich, Jülich 52425, Germany*

Hermann Tempel − *Institute of Energy Technologies (IET-1: Fundamental Electrochemistry), Forschungszentrum Jülich, Jülich 52425, Germany;* orcid.org/0000-0002-9794-6403

Rafal E. Dunin-Borkowski − *Ernst Ruska-Centre for Microscopy and Spectroscopy with Electrons (ER-C 1), Forschungszentrum Jülich GmbH, Jülich 52425, Germany;* orcid.org/0000-0001-8082-0647

Felix Hüning − *Institute of Electrical Engineering and Information Technology, FH Aachen − University of Applied Sciences, Aachen 52066, Germany*

Bing Joe Hwang − *Department of Chemical Engineering, Nano-electrochemistry Laboratory and Sustainable*

https://doi.org/10.1021/acsami.4c03729
ACS Appl. Mater. Interfaces 2024, 16, 39181−39194

Electrochemical Energy Development Center, National Taiwan University of Science and Technology, Taipei City 106, Taiwan; orcid.org/0000-0002-3873-2149

Rüdiger-A. Eichel − *Institute of Energy Technologies (IET-1: Fundamental Electrochemistry), Forschungszentrum Jülich, Jülich 52425, Germany; Institute of Physical Chemistry (IPC), RWTH Aachen University, Aachen 52066, Germany;* orcid.org/0000-0002-0013-6325

Complete contact information is available at: https://pubs.acs.org/10.1021/acsami.4c03729

Notes

The authors declare no competing financial interest.

■ ACKNOWLEDGMENTS

Beam time at the National Synchrotron Radiation Research Center (NSRRC), Taiwan, for synchrotron XAS is gratefully acknowledged. This work was financially supported by the project of "US-German Cooperation on Energy Storage" under the funding programs of "LISI-2—Lithium Solid Electrolyte Interfaces" (Project No.: 13XP0509A) and "CatSe—Interfaces and Interphases in Rechargeable Li Based Batteries: Cathode/Solid Electrolyte" (Project No.: 13XP00223A) from the Bundesministerium für Bildung und Forschung (BMBF) and "High Performance Solid-State Batteries" (HIPSTER) from "Ministerium für Kultur und Wissenschaft des Landes Nordrhein-Westfalen". Financial support by the National Council of Science and Technology under the grant MOST/NSTC 1120000023 is gratefully acknowledged.

■ REFERENCES

(1) Tsai, C.-L.; Yu, S.; Tempel, H.; Kungl, H.; Eichel, R.-A. All-ceramic Li batteries based on garnet structured Li 7 La 3 Zr 2 O 12. *Materials Technology* **2020**, *35* (9−10), 656−674.

(2) Kim, J. G.; Son, B.; Mukherjee, S.; Schuppert, N.; Bates, A.; Kwon, O.; Choi, M. J.; Chung, H. Y.; Park, S. A review of lithium and non-lithium based solid state batteries. *13th International Meeting on Lithium Batteries* **2015**, *282*, 299−322.

(3) Tsai, C.-L.; Ma, Q.; Dellen, C.; Lobe, S.; Vondahlen, F.; Windmüller, A.; Grüner, D.; Zheng, H.; Uhlenbruck, S.; Finsterbusch, M.; Tietz, F.; Fattakhova-Rohlfing, D.; Buchkremer, H. P.; Guillon, O. A garnet structure-based all-solid-state Li battery without interface modification: resolving incompatibility issues on positive electrodes. *Sustainable Energy Fuels* **2019**, *3* (1), 280−291.

(4) Tsai, C.; Thuy Tran, N. T.; Schierholz, R.; Liu, Z.; Windmüller, A.; Lin, C.; Xu, Q.; Lu, X.; Yu, S.; Tempel, H.; Kungl, H.; Lin, S.; Eichel, R.-A. Instability of Ga-substituted Li 7 La 3 Zr 2 O 12 toward metallic Li. *J. Mater. Chem. A* **2022**, *10* (20), 10998−11009.

(5) Tsai, C.-L.; Thuy Tran, N. T.; Schierholz, R.; Liu, Z.; Windmüller, A.; Lin, C.; Xu, Q.; Lu, X.; Yu, S.; Tempel, H.; Kungl, H.; Lin, S.; Eichel, R.-A. Correction: Instability of Ga-substituted Li 7 La 3 Zr 2 O 12 toward metallic Li. *J. Mater. Chem. A* **2022**, *10* (23), 12747.

(6) El Shinawi, H.; Janek, J. Stabilization of cubic lithium-stuffed garnets of the type "Li7La3Zr2O12" by addition of gallium. *J. Power Sources* **2013**, *225*, 13−19.

(7) Li, C.; Liu, Y.; He, J.; Brinkman, K. S. Ga-substituted Li7La3Zr2O12: An investigation based on grain coarsening in garnet-type lithium ion conductors. *J. Alloys Compd.* **2017**, *695*, 3744−3752.

(8) Rawlence, M.; Filippin, A. N.; Wäckerlin, A.; Lin, T.-Y.; Cuervo-Reyes, E.; Remhof, A.; Battaglia, C.; Rupp, J. L. M.; Buecheler, S. Effect of Gallium Substitution on Lithium-Ion Conductivity and Phase Evolution in Sputtered Li7−3 xGa xLa3Zr2O12 Thin Films. *ACS Appl. Mater. Interfaces* **2018**, *10* (16), 13720−13728.

(9) Rettenwander, D.; Geiger, C. A.; Tribus, M.; Tropper, P.; Amthauer, G. A synthesis and crystal chemical study of the fast ion conductor Li(7−3x)Ga(x)La3 Zr2O12 with x = 0.08 to 0.84. *Inorg. Chem.* **2014**, *53* (12), 6264−6269.

(10) Wagner, R.; Redhammer, G. J.; Rettenwander, D.; Senyshyn, A.; Schmidt, W.; Wilkening, M.; Amthauer, G. Crystal Structure of Garnet-Related Li-Ion Conductor Li7−3x Ga x La3Zr2O12: Fast Li-Ion Conduction Caused by a Different Cubic Modification? *Argonne National Lab. (ANL), Argonne, IL (United States). Advanced Photon Source (APS)* **2016**, *28* (6), 1861−1871.

(11) Yamazaki, Y.; Miyake, S.; Akimoto, K.; Inada, R. Effect of Ga2O3 Addition on the Properties of Garnet-Type Ta-Doped Li7La3Zr2O12 Solid Electrolyte. *Batteries* **2022**, *8* (10), 158.

(12) Jeong, W.; Park, S. S.; Yun, J.; Shin, H. R.; Moon, J.; Lee, J.-W. Tailoring grain boundary structures and chemistry of Li7La3Zr2O12 solid electrolytes for enhanced air stability. *Energy Storage Materials* **2023**, *54*, 543−552.

(13) Li, J.; Luo, H.; Liu, K.; Zhang, J.; Zhai, H.; Su, X.; Wu, J.; Tang, X.; Tan, G. Excellent Stability of Ga-Doped Garnet Electrolyte against Li Metal Anode via Eliminating LiGaO2 Precipitates for Advanced All-Solid-State Batteries. *ACS Appl. Mater. Interfaces* **2023**, *15* (5), 7165−7174.

(14) Huang, L.-H.; Li, C.-C. Liquid metallic Ga as sintering aid to promote the densification of garnet electrolytes for all-solid-state Li-ion batteries. *J. Power Sources* **2023**, *556*, No. 232527.

(15) Schwab, C.; Häuschen, G.; Mann, M.; Roitzheim, C.; Guillon, O.; Fattakhova-Rohlfing, D.; Finsterbusch, M. Towards economic processing of high performance garnets − case study on zero Li excess Ga-substituted LLZO. *J. Mater. Chem. A* **2023**, *11*, 5670.

(16) Su, J.; Huang, X.; Song, Z.; Xiu, T.; Badding, M. E.; Jin, J.; Wen, Z. Overcoming the abnormal grain growth in Ga-doped Li7La3Zr2O12 to enhance the electrochemical stability against Li metal. *Ceram. Int.* **2019**, *45* (12), 14991−14996.

(17) Sastre, J.; Priebe, A.; Döbeli, M.; Michler, J.; Tiwari, A. N.; Romanyuk, Y. E. Lithium Garnet Li 7 La 3 Zr 2 O 12 Electrolyte for All-Solid-State Batteries: Closing the Gap between Bulk and Thin Film Li-Ion Conductivities. *Adv. Mater. Interfaces* **2020**, *7* (17), 2000425.

(18) Chen, C.; Li, C.-A.; Yu, S.-H.; Chou, M. M. Growth and characterization of β-LiGaO2 single crystal. *J. Cryst. Growth* **2014**, *402*, 325−329.

(19) Ishii, T.; Tazoh, Y.; Miyazawa, S. Single-crystal growth of LiGaO2 for a substrate of GaN thin films. *J. Cryst. Growth* **1998**, *186* (3), 409−419.

(20) Marezio, M. The crystal structure of LiGaO 2. *Acta Crystallogr.* **1965**, *18* (3), 481−484.

(21) Limpijumnong, S.; Lambrecht, W. R. L.; Segall, B.; Kim, K. Band Structure and Cation Ordering in LiGaO2. *MRS Online Proc. Libr.* **1996**, *449*, 905.

(22) Lei, L.; Irifune, T.; Shinmei, T.; Ohfuji, H.; Fang, L. Cation order−disorder phase transitions in LiGaO2: Observation of the pathways of ternary wurtzite under high pressure. *J. Appl. Phys.* **2010**, *108* (8), 83531.

(23) Kück, S.; Hartung, S. Comparative study of the spectroscopic properties of Cr4+-doped LiAlO2 and LiGaO2. *Chem. Phys.* **1999**, *240* (3), 387−401.

(24) Brik, M. G.; Avram, C. N.; Tanaka, I. Crystal field analysis of energy level structure of LiAlO2:Cr4+ and LiGaO2:Cr4+. *phys. stat. sol. (b)* **2004**, *241* (11), 2501−2507.

(25) Lu, X.; Windmüller, A.; Schmidt, D.; Schöner, S.; Schierholz, R.; Tsai, C.-L.; Kungl, H.; Liao, X.; Yu, S.; Tempel, H.; Chen, Y.; Eichel, R.-A. Disentangling Phase and Morphological Evolution During the Formation of the Lithium Superionic Conductor Li10 GeP2 S12. *Small (Weinheim an der Bergstrasse, Germany)* **2023**, *19*, No. e2300850.

(26) Rietveld, H. M. A profile refinement method for nuclear and magnetic structures. *J. Appl. Crystallogr.* **1969**, *2* (2), 65−71.

(27) Wondratschek, H.; Müller, U.; Wondratschek, H.; Müller, U., Eds. *International tables for crystallography*, 2. ed., *A1*; Wiley, 2010. DOI: .
(28) Kabelka, H.; Kuzmany, H.; Krempl, P. Raman scattering of LiGaO2. *Solid State Commun.* **1978**, *27* (11), 1159−1162.
(29) Boonchun, A.; Dabsamut, K.; Lambrecht, W. R. L. First-principles study of point defects in LiGaO 2. *J. Appl. Phys.* **2019**, *126* (15), 155703.
(30) Boonchun, A.; Lambrecht, W. R. L. First-principles study of the elasticity, piezoelectricity, and vibrational modes in LiGaO2 compared with ZnO and GaN. *Phys. Rev. B* **2010**, *81* (23), No. 235214.
(31) Matyi, R. J.; Doolittle, W. A.; Brown, A. S. High resolution x-ray diffraction analyses of GaN/LiGaO2. *J. Phys. D: Appl. Phys.* **1999**, *32* (10A), A61−A64.
(32) Chen, J.; Fang, W.; Ao, L.; Tang, Y.; Li, J.; Liu, L.; Fang, L. Structure and chemical bond characteristics of two low-ε microwave dielectric ceramics LiBO2 (B = Ga, In) with opposite τ. *Journal of the European Ceramic Society* **2021**, *41* (6), 3452−3458.
(33) Marezio, M.; Remeika, J. P. High pressure phase of LiGaO2. *J. Phys. Chem. Solids* **1965**, *26* (8), 1277−1280.
(34) Windmüller, A.; Tsai, C.-L.; Möller, S.; Balski, M.; Sohn, Y. J.; Uhlenbruck, S.; Guillon, O. Enhancing the performance of high-voltage LiCoMnO4 spinel electrodes by fluorination. *J. Power Sources* **2017**, *341*, 122−129.
(35) Windmüller, A.; Renzi, T.; Kungl, H.; Taranenko, S.; Suard, E.; Fauth, F.; Duttine, M.; Tsai, C.-L.; Sun, R.; Durmus, Y. E.; Tempel, H.; Jakes, P.; Masquelier, C.; Eichel, R.-A.; Croguennec, L.; Ehrenberg, H. Feasibility and Limitations of High-Voltage Lithium-Iron-Manganese Spinels. *J. Electrochem. Soc.* **2022**, *169* (7), 70518.
(36) Guo, J.; Gao, F.; Li, D.; Luo, X.; Sun, Y.; Wang, X.; Ran, Z.; Wu, Q.; Li, S. Novel Strategy of Constructing Hollow Ga 2 O 3 @N-CQDs as a Self-Healing Anode Material for Lithium-Ion Batteries. *ACS Sustainable Chem. Eng.* **2020**, *8* (36), 13692−13700.
(37) Huang, Y.; Tang, X.; Wang, J.; Ma, H.; Wang, Y.; Liu, W.; Wang, G.; Xiao, L.; Lu, J.; Zhuang, L. Two-Dimensional Ga2O3/C Nanosheets as Durable and High-Rate Anode Material for Lithium Ion Batteries. *Langmuir* **2019**, *35* (42), 13607−13613.
(38) Tang, X.; Huang, X.; Huang, Y.; Gou, Y.; Pastore, J.; Yang, Y.; Xiong, Y.; Qian, J.; Brock, J. D.; Lu, J.; Xiao, L.; Abruña, H. D.; Zhuang, L. High-Performance Ga2O3 Anode for Lithium-Ion Batteries. *ACS Appl. Mater. Interfaces* **2018**, *10* (6), 5519−5526.
(39) Lei, L.; Ohfuji, H.; Qin, J.; Zhang, X.; Wang, F.; Irifune, T. High-pressure Raman spectroscopy study of LiGaO2. *Solid State Commun.* **2013**, *164*, 6−10.
(40) Sappl, J.; Hoch, C. Synthesis and Crystal Structure of Three Ga-rich Lithium Gallides, LiGa6, Li11Ga24, and LiGa2. *Inorg. Chem.* **2020**, *59* (9), 6566−6580.
(41) Schulz, H.; Schwarz, K. Is there an N 3− ion in the crystal structure of the ionic conductor lithium nitride (Li 3 N)? *Acta Cryst. A* **1978**, *34* (6), 999−1005.
(42) Stöhr, J.; Schäfer, H. Darstellung und Struktur von Li 5 Ga 4. *Z. anorg. allg. Chem.* **1981**, *474* (3), 221−225.
(43) Voronin, V. I.; Berger, I. F.; Proskurnina, N. V.; Goschitskii, B. N. Defects in a lattice of pure nickel subjected to fast-neutron irradiation followed by annealings: Neutron-diffraction examination. *Phys. Metals Metallogr.* **2016**, *117* (4), 348−354.
(44) Yao, Y.; Ishikawa, Y.; Sugawara, Y. X-ray diffraction and Raman characterization of β-Ga 2 O 3 single crystal grown by edge-defined film-fed growth method. *J. Appl. Phys.* **2019**, *126* (20), 205106.
(45) Onuma, T.; Fujioka, S.; Yamaguchi, T.; Itoh, Y.; Higashiwaki, M.; Sasaki, K.; Masui, T.; Honda, T. Polarized Raman spectra in β-Ga2O3 single crystals. *J. Cryst. Growth* **2014**, *401*, 330−333.
(46) Kranert, C.; Sturm, C.; Schmidt-Grund, R.; Grundmann, M. Raman tensor elements of β-Ga2O3. *Sci. Rep.* **2016**, *6* (1), 35964.
(47) Janzen, B. M.; Mazzolini, P.; Gillen, R.; Peltason, V. F. S.; Grote, L. P.; Maultzsch, J.; Fornari, R.; Bierwagen, O.; Wagner, M. R. Comprehensive Raman study of orthorhombic κ/ε-Ga 2 O 3 and the impact of rotational domains. *J. Mater. Chem. C* **2021**, *9* (40), 14175−14189.
(48) Creighton, J. A.; Withnall, R. The Raman spectrum of gallium metal. *Chem. Phys. Lett.* **2000**, *326* (3−4), 311−313.
(49) Taklu, B. W.; Nikodimos, Y.; Bezabh, H. K.; Lakshmanan, K.; Hagos, T. M.; Nigatu, T. A.; Merso, S. K.; Sung, H.-Y.; Yang, S.-C.; Wu, S.-H.; Su, W.-N.; Hwang, B. J. Air-stable iodized-oxychloride argyrodite sulfide and anionic swap on the practical potential window for all-solid-state lithium-metal batteries. *Nano Energy* **2023**, *112*, No. 108471.
(50) Wood, K. N.; Teeter, G. XPS on Li-Battery-Related Compounds: Analysis of Inorganic SEI Phases and a Methodology for Charge Correction. *ACS Appl. Energy Mater.* **2018**, *1* (9), 4493−4504.
(51) Zhou, Y.; Zhang, J.; Zhao, K.; Ma, Y.; Zhang, H.; Song, D.; Shi, X.; Zhang, L.; Ding, Y. A novel dual-protection interface based on gallium-lithium alloy enables dendrite-free lithium metal anodes. *Energy Storage Materials* **2021**, *39*, 403−411.
(52) Chowdhury, T. A. XPS Depth Profile Study of Sprayed Ga_2O_3 Thin Films. *ENG* **2023**, *15* (08), 459−466.
(53) Han, W.; Kohler-Redlich, P.; Ernst, F.; Rühle, M. Growth and microstructure of Ga2O3 nanorods. *Solid State Commun.* **2000**, *115* (10), 527−529.
(54) Shang, L.; Wang, Y.; Zhuang, M.; Liu, B.; Shi, F. Growth behavior of β -Ga 2 O 3 nanowires synthesized by chemical vapor deposition. *Mater. Res. Express* **2019**, *6* (11), 1150a5.
(55) Jain, A.; Ong, S. P.; Hautier, G.; Chen, W.; Richards, W. D.; Dacek, S.; Cholia, S.; Gunter, D.; Skinner, D.; Ceder, G.; Persson, K. A. Commentary: The Materials Project: A materials genome approach to accelerating materials innovation. *APL Mater.* **2013**, *1* (1), No. 011002.
(56) Patel, A. M.; Nørskov, J. K.; Persson, K. A.; Montoya, J. H. Efficient Pourbaix diagrams of many-element compounds. *Phys. Chem. Chem. Phys.* **2019**, *21* (45), 25323−25327.
(57) Persson, K. A.; Waldwick, B.; Lazic, P.; Ceder, G. Prediction of solid-aqueous equilibria: Scheme to combine first-principles calculations of solids with experimental aqueous states. *Phys. Rev. B* **2012**, *85* (23), No. 235438.
(58) Singh, A. K.; Zhou, L.; Shinde, A.; Suram, S. K.; Montoya, J. H.; Winston, D.; Gregoire, J. M.; Persson, K. A. Electrochemical Stability of Metastable Materials. *Argonne National Lab. (ANL), Argonne, IL (United States). Advanced Photon Source (APS)* **2017**, *29* (23), 10159−10167.
(59) Priyantha, W.; Radhakrishnan, G.; Droopad, R.; Passlack, M. In-situ XPS and RHEED study of gallium oxide on GaAs deposition by molecular beam epitaxy. *J. Cryst. Growth* **2011**, *323* (1), 103−106.